SOLAR ENERGY

Light-induced picosecond rotational disordering of the inorganic sublattice in hybrid perovskites

Xiaoxi Wu,[1] Liang Z. Tan,[2] Xiaozhe Shen,[3] Te Hu,[4] Kiyoshi Miyata,[5] M. Tuan Trinh,[5] Renkai Li,[3] Ryan Coffee,[3] Shi Liu,[6] David A. Egger,[7] Igor Makasyuk,[3] Qiang Zheng,[3] Alan Fry,[3] Joseph S. Robinson,[3] Matthew D. Smith,[8] Burak Guzelturk,[1] Hemamala I. Karunadasa,[8] Xijie Wang,[3] Xiaoyang Zhu,[5] Leeor Kronik,[7] Andrew M. Rappe,[2] Aaron M. Lindenberg[1,4,9]*

Femtosecond resolution electron scattering techniques are applied to resolve the first atomic-scale steps following absorption of a photon in the prototypical hybrid perovskite methylammonium lead iodide. Following above-gap photoexcitation, we directly resolve the transfer of energy from hot carriers to the lattice by recording changes in the mean square atomic displacements on 10-ps time scales. Measurements of the time-dependent pair distribution function show an unexpected broadening of the iodine-iodine correlation function while preserving the Pb–I distance. This indicates the formation of a rotationally disordered halide octahedral structure developing on picosecond time scales. This work shows the important role of light-induced structural deformations within the inorganic sublattice in elucidating the unique optoelectronic functionality exhibited by hybrid perovskites and provides new understanding of hot carrier—lattice interactions, which fundamentally determine solar cell efficiencies.

INTRODUCTION

As a new prototype material for next-generation high-efficiency and low-cost thin-film solar cells, methylammonium lead iodide ($MAPbI_3$) has become a "super star" in the solar cell community since 2010 (*1*–*4*). Although perovskite solar cell efficiencies have climbed above the 20% mark (*5*, *6*), the fundamental working mechanism responsible for these efficiencies and the associated long carrier lifetimes is not understood (*7*, *8*). $MAPbI_3$ has an organic-inorganic hybrid structure, where PbI_3^--based octahedra compose the fundamental building blocks and MA^+ cations fill the interstices (Fig. 1). Recent studies probing the unique aspects of charge carrier generation and transport exhibited by these materials have focused on the roles of (i) dynamic structural fluctuations, associated with ultrafast changes in local band structure and centrosymmetry, in facilitating charge separation and hindering recombination (*9*–*13*) and (ii) the motion of organic cations in screening and protecting carriers from trapping and recombination (*14*–*19*).

Until now, most of the photophysical studies have been based on optical measurements, which probe dipole-allowed electronic transitions with high time resolution but only indirectly probe the nuclear response. Static x-ray and transmission electron microscopy (TEM) studies have been reported (*20*–*23*) but compete with fast sample degradation (*24*, *25*). Time-resolved neutron-scattering experiments provide specific information on the organic dipole orientation based on spin magnetic interactions (*26*). Compared to x-ray and neutron scattering, electrons interact with nuclei more strongly and thus facilitate the detection of relatively weak diffuse scattering, from which information about unit cell deformations may be extracted (*27*–*29*). Here, we report the first direct real-time measurement of the dynamical structural processes that follow absorption of above-gap photons in $MAPbI_3$ perovskite thin films using megaelectron volt ultrafast electron diffraction (UED). With this technique, we visualize the lattice response associated with the hot carrier–lattice thermalization process, one of the key energy loss channels that determine the efficiency of a solar cell. Furthermore, analysis of the differential pair distribution function (PDF), extracted from the dynamical evolution of the diffraction spectra, reveals that the dominant atomic motion in the inorganic lattice occurs within the iodine octahedra, as manifested in a large-amplitude light-induced broadening of the I–I correlation function on picosecond time scales. Meanwhile, the Pb–I distances are preserved within the signal-to-noise ratio of our measurement. Our observation therefore indicates that above-gap photoexcitation induces significant rotational sublattice disorder of the iodine octahedra, associated with changes of the I–Pb–I bond angles.

RESULTS AND DISCUSSION

The UED experimental setup is illustrated in Fig. 1, and a typical static diffraction image from $MAPbI_3$ thin film is shown in the inset. The diffraction pattern is composed of a series of concentric rings associated with an ensemble of crystalline grains (~50 to 100 nm in size) with random orientation. After azimuthal integration, a plot of diffracted intensity I versus Q (where $Q_{hkl} = \frac{2\pi}{d_{hkl}}$ is the momentum transfer of the scattered electron) is acquired. The indices of the diffraction peaks are listed in table S1, and the measured diffraction spectrum is overlaid with the simulated electron diffraction spectrum in fig. S1. Our experimental Q resolution of ≈0.17 $Å^{-1}$ (determined from measurements on single-crystal gold) is not high enough to resolve all adjacent peaks. We denote the peaks as nos. 1 to 8 for convenience in the following discussion.

To study the carrier-lattice interaction, we first pumped the perovskite thin film with above-gap 400-nm photons and recorded diffraction

[1]Stanford Institute for Materials and Energy Sciences, SLAC National Accelerator Laboratory, Menlo Park, CA 94025, USA. [2]The Makineni Theoretical Laboratories, Department of Chemistry, University of Pennsylvania, Philadelphia, PA 19104–6323, USA. [3]SLAC National Accelerator Laboratory, Menlo Park, CA 94025, USA. [4]Department of Materials Science and Engineering, Stanford University, Stanford, CA 94305, USA. [5]Department of Chemistry, Columbia University, New York, NY 10027, USA. [6]Extreme Materials Initiative, Geophysical Laboratory, Carnegie Institution for Science, Washington, DC 20015, USA. [7]Department of Materials and Interfaces, Weizmann Institute of Science, Rehovoth 76100, Israel. [8]Department of Chemistry, Stanford University, Stanford, CA 94305, USA. [9]PULSE Institute, SLAC National Accelerator Laboratory, Menlo Park, CA 94025, USA.
*Corresponding author. Email: aaronl@stanford.edu

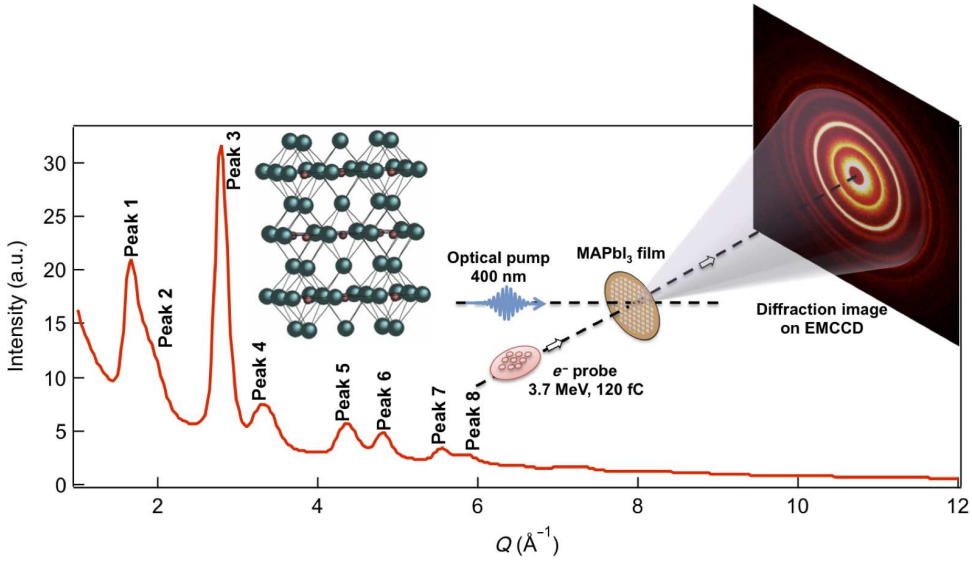

Fig. 1. Radial diffraction intensity plot as a function of scattering vector *Q*. Center inset: Atomic-scale structure of $MAPbI_3$ with tetragonal phase and *I*4*cm* space group (dark green spheres denote I and red spheres denote Pb). Right inset: Schematic of femtosecond transmission electron diffraction setup with optical pump and electron probe, showing also the recorded two-dimensional diffraction image of the $MAPbI_3$ perovskite thin film. a.u., arbitrary units; EMCCD, electron-multiplying charge-coupled device.

images for different time delays between a pump and a probe. Snapshots of the time-resolved peak intensities and differential scattering dynamics are plotted in Figs. 2A and 3 (inset), respectively. After photoexcitation with a 400-nm pump, we observed two clear effects: (i) The relative intensities of all Bragg peaks decrease and (ii) the scattering in regions in between the main Bragg peaks increases. As shown in Fig. 2A, the relative intensity drop has a clear *Q* dependence: Higher-order peaks show larger decreases. Figure 2C shows that the logarithm of the intensity modulation for a particular Bragg peak depends nearly linearly on the corresponding Q^2 for this Bragg peak; that is, it follows a Debye-Waller–like dependence: $I(Q,t) \propto \exp\left(-\frac{1}{3}Q^2\left\langle u^2_{\mathrm{RMS}}(t)\right\rangle\right)$, where $\left\langle u^2_{\mathrm{RMS}}(t)\right\rangle$ is the time-dependent mean square displacement of the atoms [RMS (root mean square)] (*30*, *31*). The peak intensity decay is correlated with the rise of the lattice temperature (for small changes in diffraction intensity), with a measured time constant of 10 ± 1 ps under an excitation fluence of 66 μJ/cm^2, corresponding to an estimated carrier density of 2.3×10^{19} cm^{-3} (see the Supplementary Materials). Photoexcitation at 400 nm generates electrons and holes that first equilibrate at an elevated carrier temperature T_e within hundreds of femtoseconds through carrier-carrier scattering before relaxing to the band edge via carrier-phonon scattering and transferring their excess electronic energy to the lattice (*32*, *33*). Thus, the dynamics of the peak intensity decay track the hot-carrier cooling time scale (*31*). After ≈10 ps, both the carriers and the lattice reach an equilibrium, and no further thermalization is observed (figs. S2D and S3). From the *Q*-dependent Bragg peak intensity drop, one may extract the photoinduced change in the RMS $\left(\sqrt{\left\langle u^2_{\mathrm{RMS}}(t)\right\rangle}\right)$ displacements under the assumption of isotropic disorder (*31*). Maximum observed RMS displacements are ≈0.1 Å for temperature jumps of ≈8 K (see the Supplementary Materials), showing that weak photoexcitation induces large structural deformations. From a Debye model, we estimate an effective Debye temperature $\theta_D \approx 60$ K (table S2), comparable with both experimental values from heat capacity measurements (*20*) and theoretical calculations (*34*). To further validate the correspondence between changes in the RMS displacements and lattice temperature, we performed classical molecular dynamics (MD) simulations (see Materials and Methods). Figure 2D shows that the experimental RMS displacement changes agree well with the results extracted from the force field MD simulations.

To explore explicitly how the band-edge carriers interact with the lattice, we tuned the pump wavelength to 700 nm, close to the band gap of 760 nm. Contrary to the effects observed under 400-nm excitation, we only observed <1% Bragg peak intensity changes even at the highest fluence measured of order 4.3×10^{19}/cm^3, just below the damage threshold (≈230 μJ/cm^2) and corresponding to similar carrier densities as measured under 400-nm excitation. This indicates that cold carrier–defect scattering in perovskites leads to negligible lattice heating, which is consistent with reported transport measurements and shows that the dominant heating response comes from hot carrier/phonon coupling (*16*, *35*, *36*).

Analysis based on the Bragg peaks effectively averages over all atoms, with dominant contributions from the Pb and I atoms. More information on the pump-induced structural changes can be obtained by analyzing the scattering in between the main Bragg peaks (*29*, *37*). Figure 3 shows that the loss of Bragg peak diffraction intensity leads to a gain in the intensity between peaks. The dynamics of the scattering averaged over different *Q* regions are plotted in the inset of Fig. 3, showing that low-*Q* scattering (Q_1 = 2.1 to 2.6 Å^{-1} and Q_2 = 3.8 to 4.1 Å^{-1}) rises more slowly than higher-*Q* scattering (Q_3 = 5.1 to 5.3 Å^{-1} and Q_4 = 6.1 to 6.8 Å^{-1}) in contrast to the Bragg peak dynamics (which show similar time evolution for all peaks; figs. S5 and S6 and table S3). To check whether thermal effects and/or heating across the known tetragonal-to-cubic phase transition (typically occurring at temperatures significantly higher than that induced here) are playing a role in the observed effects, we carried out temperature-dependent x-ray scattering studies of crystalline powders of $MAPbI_3$, as described in the Supplementary Materials. These measurements show effects consistent with previous studies (*38*–*40*) but not consistent with the differential changes

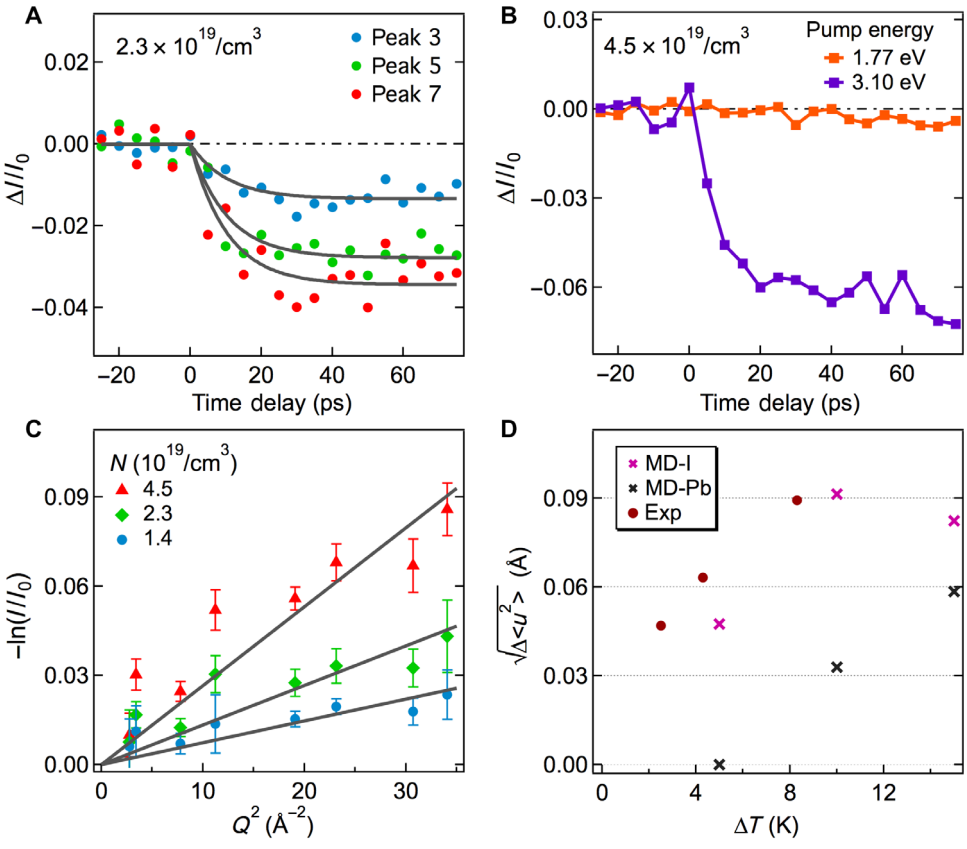

Fig. 2. Time-dependent changes in Bragg peak intensities and associated RMS displacements. (**A**) Peak intensity dynamics for different diffraction peaks showing *Q*-dependent peak intensity decay with similar time constants. Excitation is at 400 nm and corresponding to a carrier density of 2.3×10^{19}/cm^3. The solid curves are global fits. Global fitting results for other peaks are plotted in fig. S7. (**B**) Comparison of peak no. 7 decay between 400- and 700-nm pump with similar photoinduced carrier density. (**C**) Semilog plot of intensity change (signal averaged over a delay range of 40 to 75 ps) as a function of the squared scattering factor (Q^2) for different excitation densities, showing a Debye-Waller–like response corresponding to an increase in the RMS displacements of the atoms. The solid lines are linear fits with *y* intercept forced to 0. (**D**) Comparison between experimental and theoretical RMS ($\sqrt{\langle u^2_{\mathrm{RMS}} \rangle}$ in angstroms) displacements at different temperatures (ΔT is referenced to room temperature).

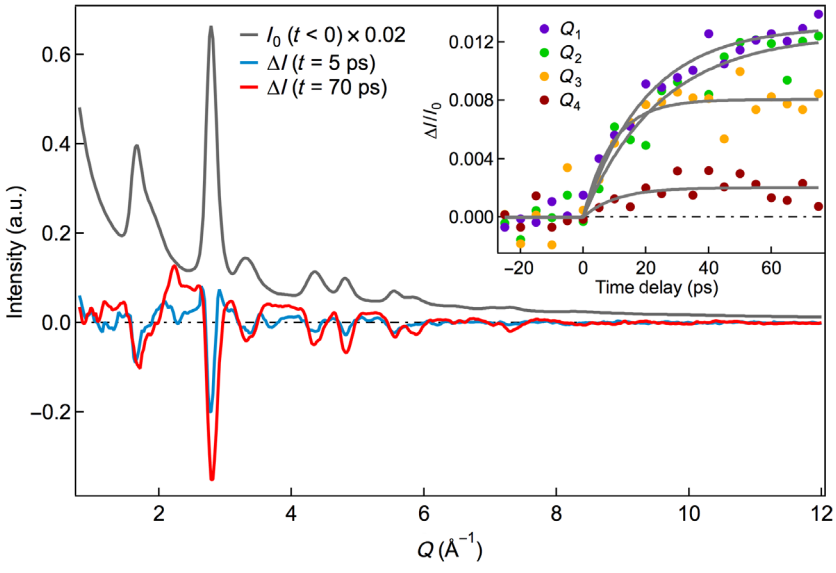

Fig. 3. Static and differential radial diffraction spectra at different time delays. Differential radial diffraction spectrum at $t = 5$ and 70 ps with a photoexcited carrier density of 2.3×10^{19}/cm^3. Inset: Time evolution of scattering integrated over four different *Q* ranges: Q_1 = (2.1 to 2.6 Å^{-1}), Q_2 = (3.8 to 4.1 Å^{-1}), Q_3 = (5.1 to 5.3 Å^{-1}), and Q_4 = (6.1 to 6.8 Å^{-1}). The solid curves are single exponential fits to each *Q* range with time constants of 20 (±2) ps, 25 (±5) ps, 9 (±3) ps, and 11 (±7) ps from low *Q* to high *Q*, respectively.

shown in Fig. 3. This indicates that additional optically induced structural deformations other than pure thermal effects are occurring, which is discussed further below.

From a Fourier transform of the differential diffraction spectrum, one may extract the pump-induced change in the PDF, reflecting changes in local correlations at the atomic scale (for details, see the Supplementary Materials). Static PDF analysis on $MAPbI_3$ based on x-ray scattering studies has been reported, showing peaks at $r \approx 3.2$ Å and $r \approx 4.6$ Å, corresponding to the nearest-neighbor Pb–I and I–I pairs, respectively (*22*). The pump-induced changes in the PDF at different time delays are plotted in Fig. 4. A clear negative feature at $r \approx 4.6$ Å, the nearest-neighbor I–I distance, along with two positive features on either side, is observed. This is an indication of I–I PDF peak broadening, occurring a result of variations in the distance between nearest-neighbor iodine ions which make up the octahedron around each Pb atom. In contrast, no differential PDF signal is observed at $r \approx 3.2$ Å, the nearest Pb–I distance. Together, these observations indicate a rotational disordering of the I atoms on a spherical surface around the Pb center within each PbI_6^{4-} octahedron. From the peak magnitude of the change in the PDF, we estimate a light-induced broadening of the I–I correlation function by ~0.1 Å (see the Supplementary Materials), an amount comparable to its initial intrinsic width and consistent with the magnitudes estimated from the simple Debye-Waller analysis.

In $MAPbI_3$, we find that the time scale for the change in the PDF (27 ± 8 ps) is significantly slower than the Bragg peak intensity drop (10 ± 1 ps) for a carrier density of $2.3 \times 10^{19}/cm^3$. Additionally, this time constant is observed to be excitation intensity–dependent, with faster effects observed for higher carrier density (inset of Fig. 4A). These discrepancies in rates, along with the observed deviations from simple Debye-Waller–like responses at low Q, suggest that the origin of the observed rotational disordering is not merely due to thermally activated processes. Further support for this statement comes from our MD simulations. The equilibrium change in PDF, ΔG, calculated from MD trajectories at 300 and 325 K, shows that pure isotropic thermal fluctuations are unlikely to cause this large selective broadening of the I–I PDF peak (Fig. 4B). The MD calculations, in contrast, show similar broadening of both Pb–I and I–I peaks and predict changes in the I–I PDF peak significantly smaller than observed

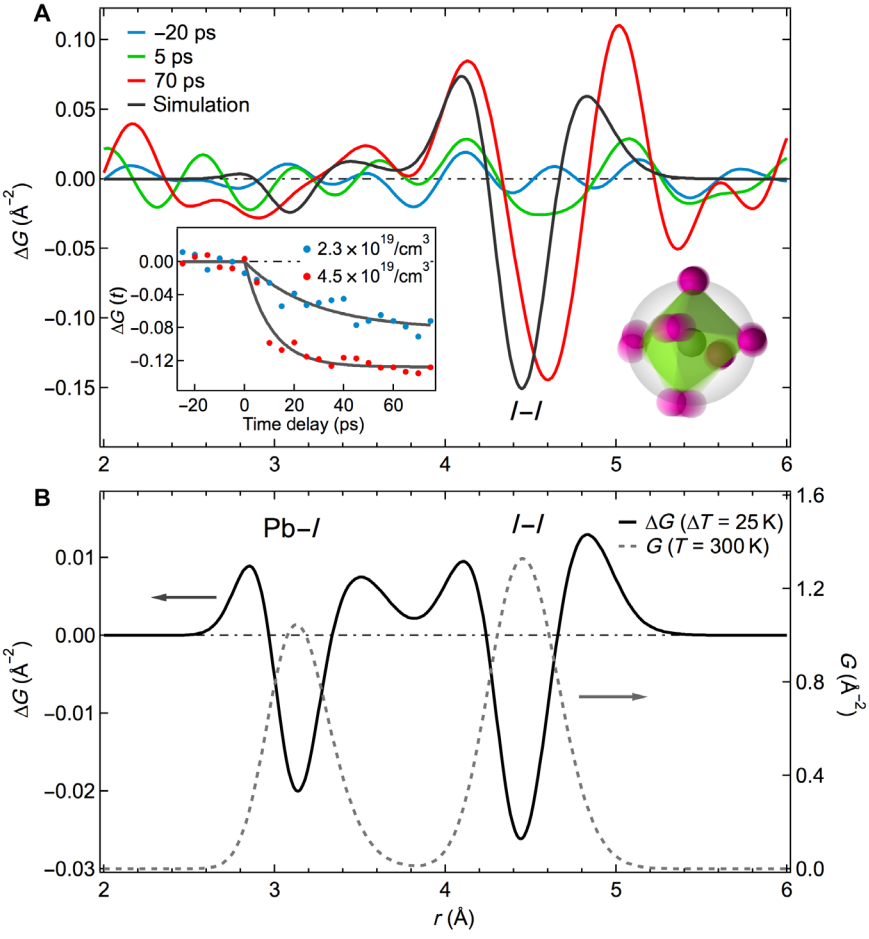

Fig. 4. Comparison between experimental and calculated differential PDF. (**A**) Differential PDF at different delay times with a carrier density of $4.5 \times 10^{19}/cm^3$. The black curve in the main panel is the calculated difference PDF from MD simulations equilibrated at temperatures 300 and 325 K ($\Delta T = 25$ K), with additional fluctuations of iodine atoms 0.1 Å in magnitude, to simulate the photoactivation (see text for details). Left inset shows the time-dependent PDF dynamics at $r = 4.6$ (±0.1) Å corresponding to the I–I atomic distance under two excitation densities, as noted in the figure. The solid curves in the left inset are single exponential fits. Right inset is an illustration of the proposed I rotational disorder in one PbI_6 octahedron. (**B**) Calculated PDF (solid line) at room temperature (300 K; left axis) and calculated difference PDF (dashed line) from MD simulations equilibrated at temperatures 300 and 325 K, without additional fluctuations, corresponding to pure thermal activation.

experimentally. Similar results were obtained for MD simulation temperatures up to 400 K (fig. S9). We estimate the additional fluctuation required to explain the experimental results by adding post hoc random displacements to our MD trajectories and calculating the resulting PDFs. We add independent normally distributed displacements of magnitude 0.1 Å to iodine atoms in directions perpendicular to Pb–I bonds and find good agreement with experimental PDF in both the shape and the amplitude (Fig. 4A). The 0.1 Å I displacement also agrees with the broadening of the I–I correlation function estimated above from the experimental PDF analysis. This implies that light preferentially excites volume-preserving distortions of I_6 cages (deviations of the I–Pb–I bond angle) around the Pb center in each PbI_6^{4-} octahedron. Additional contributions may come from tilting of adjacent octahedra. From the magnitude of the experimentally or theoretically estimated displacements, this corresponds to an angular deviation of a few degrees, comparable to that estimated theoretically by Motta *et al.* (*11*). We carried out similar time-resolved PDF analysis on gold polycrystalline films, which exhibit a simple homogeneous lattice heating response upon photoexcitation, and observed isotropic broadening responses at all nearest-neighbor distances, confirming the validity of our PDF analysis (fig. S10).

CONCLUSION

We conclude by briefly discussing the significance of and the physical mechanisms for the observed changes in the PDF. Recent studies have emphasized the role of structural fluctuations in reducing effective bimolecular recombination constants in the hybrid perovskites, typically in reference to the freely reorienting organic dipoles (MA^+) and their coupling to the inorganic lattice (*11*, *19*). Our work shows that one should consider not only the organic molecules but also the contribution from the inorganic lattice and, in particular, the structural deformations induced by absorption of a photon. Indeed, the I–I correlation peak broadens by an amount comparable to its intrinsic width (under excitation conditions corresponding to temperature jumps of <10 K). Considering that these distortions are localized within each octahedron and our UED experiment averages over all unit cells in the sample, the extracted I–I broadening is likely an underestimate of the local motions near an excited carrier.

The MD simulations demonstrate that equilibrium thermal activation cannot explain the observed distortion. From the fact that no clear Pb–I correlation change was observed even after ~200 ps (fig. S11), we further conclude that the observed effect is not due to nonequilibrated thermal excitation (for example, preferential excitation of I before eventually coupling to Pb). This indicates that the distortions of the I ions likely arise from electronic excitation and are frozen within the I sublattice. A light-induced hydrogen bond–breaking mechanism between MA^+ and I^- has recently been hypothesized with respect to photoenhanced lattice expansion, H migration via the Bourgoin-Corbett mechanism, and ferroelectric response in the hybrid perovskites (*14*, *41*–*43*). The observation that the I-sublattice distortion stabilizes faster under higher pump fluence (inset of Fig. 4A) and only occurs under above-gap excitation is consistent with the presence of an activation barrier for the distortion, where higher carrier temperatures help to overcome the barrier faster. The observed dominant motion of the iodine is also consistent with previous predictions that I^- ions have the smallest hopping barriers among the intrinsic defect species and that ionic transport processes may be light-enhanced (*44*–*46*), but we emphasize that, on the short times probed here, all observed effects are reversible at the 180-Hz repetition rate of the experiment and do not lead to full ionic hops. Future studies under lower excitation density (closer to 1-sun illumination) that probe the observed short-time ionic displacements and their dependence on sample morphology may help to explain morphology-dependent device performance. Finally, this light-enhanced local disorder provides a source for the structural reorganizations that underlie light-induced changes in dielectric constant (*19*, *47*) and the dynamical symmetry breaking required for proposed Rashba effects and other photoinduced changes in band structure (*9*, *11*, *13*). From these perspectives, although structural fluctuations may facilitate charge separation and ion transport, these also depend on the carrier generation process, which further softens the lattice and makes it even more vulnerable to deformation.

MATERIALS AND METHODS

Ultrafast electron diffraction

The UED experimental setup is illustrated in Fig. 1 and is similar to that reported elsewhere (*31*, *37*, *48*). The output of a multipass-amplified Ti:sapphire laser was split into two paths: one doubled to 400 nm as the pump and the other tripled for the electron pulse generation. Alternatively, for 700-nm pump excitation, the pump beam was first frequency-converted using an optical parameter amplifier. The electron pulses were accelerated to 3.7 MeV with 300-fs [full width at half maximum (FWHM), estimated by N-body simulation for ~120 fC per pulse] duration in the SLAC UED facility (*47*). Electron pulses were focused onto the $MAPbI_3$ films at normal incidence with a ~300-μm diameter, and the diffracted electrons were detected by a red phosphor screen and captured using an electron-multiplying charge-coupled device. The pump beam with 40-fs (FWHM) duration was spatially overlapped with the electron beam on the sample with an incident angle of ~3° and a diameter of ~400 μm. The pump beam and the electron probe beam were phase-locked and synchronized at 180 Hz. The delay between the pump and probe pulses was controlled by a translational stage. All data discussed above were taken on fresh samples without observable sample degradation. At the highest fluence investigated and after several hours of photoexcitation, some evidence for degradation and production of PbI_2 (fig. S15, peak 4 of PbI_2) was observed, which was used as a monitor of the sample stability.

MD simulations

Classical MD simulations were performed on an 8 × 8 × 8 pseudocubic supercell of $MAPbI_3$ (6144 atoms, one formula unit in each pseudocubic unit cell) with the LAMMPS (Large-scale Atomic/Molecular Massively Parallel Simulator) code (*49*). We used the force field developed by Mattoni *et al.* (*50*), which was shown to provide an accurate description of temperature-dependent lattice expansion and orthorhombic-to-tetragonal phase sequences of $MAPbI_3$. The good agreement between simulations and experiments, as shown in Fig. 2D, on the changes in RMS displacements at different temperatures, along with the agreement of the calculated bond lengths, RMS displacements (table S5), and Pb–I and I–I PDF peak widths (Fig. 4B) with literature values (*22*, *51*), further confirmed the validity of the MD simulations. Starting from 300 K, we increased the simulation temperature in 5-K steps to mimic experimental temperature jumps using a Nosé-Hoover thermostat. At each temperature, we first equilibrated the system using an NPT (isothermal-isobaric) ensemble and ≈500-ps simulation time and then performed a 20-ps NVT (canonical)

production run to extract the structural data; the time step in all cases was set to 0.5 fs.

Perovskite thin-film growth

Thin films of lead halide perovskite (~40 nm) were prepared by thermal evaporation of methylammonium iodide (MAI) and $PbCl_2$ in high vacuum (base pressure $<10^{-5}$ Pa). The materials were codeposited onto a TEM grid supported by a 20-nm carbon film. The partial pressure of MAI was maintained at $\sim 2 \times 10^{-3}$ Pa during evaporation. The substrate was at room temperature during growth, and each sample was postannealed in MAI atmosphere at 370 K for 15 min. The deposition rate of $PbCl_2$ was ~0.5 nm/min, as monitored by a quartz crystal microbalance (*1*). PbI_2 thin films were spin-coated on 50-nm SiN windows. Each diffraction image frame was accumulated over 540 electron pulses (3 s), and at each pump-probe time delay, three image frames were taken. In addition to the time-resolved diffraction images taken with pump and probe pulses at a certain given time delay, we also recorded the static diffraction images at each delay position without pump irradiation, which was used as a reference for sample damage.

SUPPLEMENTARY MATERIALS

Supplementary material for this article is available at http://advances.sciencemag.org/cgi/content/full/3/7/e1602388/DC1

Supplementary Text

fig. S1. Overlay of simulated electron scattering pattern and the measured diffraction pattern.

fig. S2. Transient absorption data and analysis for $MAPbI_3$.

fig. S3. Long-time dynamics for high-order Bragg peaks of perovskite thin films for two photoexcited carrier densities.

fig. S4. Scanning electron microscopy images of thermally evaporated perovskite thin films on TEM grids, showing an averaged grain size of about 50 to 100 nm.

fig. S5. Pump fluence dependence of Bragg peak 1 to 4 (markers) intensity decay and single exponential fits (gray lines) to peaks 3 and 4.

fig. S6. Pump fluence dependence of Bragg peak 5 to 8 (markers) intensity decay and single exponential fits (gray lines) to each peak.

fig. S7. Global fitting of time-dependent intensity for peaks not shown in Fig. 2.

fig. S8. Gaussian fit peak center change as function of pump-probe time delay for two photoexcited carrier densities.

fig. S9. Calculated PDF difference between MD simulation temperatures T = 400 K and T = 375 K.

fig. S10. Differential PDF plots of gold polycrystalline thin film at different time delays.

fig. S11. Differential PDF plots at long-time delays under excitation at 400 nm with a carrier density of $2.3 \times 10^{19}/cm^3$.

fig. S12. Differential PDF plots at different time delays under excitation at 400 nm with a carrier density of $4.5 \times 10^{19}/cm^3$.

fig. S13. Differential PDF plots at different time delays under excitation at 400 nm with a carrier density of $2.3 \times 10^{19}/cm^3$.

fig. S14. Differential PDF plots at different time delays under excitation at 400 nm with a carrier density of $1.4 \times 10^{19}/cm^3$.

fig. S15. Comparison between electron diffraction on $MAPbI_3$ and PbI_2 thin films.

fig. S16. Absorption spectra of $MAPbI_3$ and PbI_2; PbI_2 time-resolved diffraction response.

fig. S17. Differential PDF plots of PbI_2 thin films at different time delays.

fig. S18. Temperature-dependent x-ray diffraction scans across the tetragonal-cubic phase transition in $MAPbI_3$ (measured from crystalline powders).

fig. S19. Zoom-in evolution of diffraction peaks across the tetragonal-cubic phase transition.

fig. S20. Intensity of (211) reflection as a function of temperature showing gradual decrease in intensity during the tetragonal-cubic transition.

fig. S21. Normalized changes in area for selected diffraction peaks shown in fig. S18 as a function of temperature.

table S1. Index of diffraction peaks.

table S2. Summary of carrier density, ΔT, mean square displacement, and Debye temperature.

table S3. Summary of decay time constants in picoseconds from single exponential fits of individual peaks under different pump fluences.

table S4. Gaussian fit peak centers for eight peaks.

table S5. Calculated atomic RMS in angstroms at different temperatures.

References (*52*–*56*)

REFERENCES AND NOTES

1. M. Liu, M. B. Johnston, H. J. Snaith, Efficient planar heterojunction perovskite solar cells by vapour deposition. *Nature* **501**, 395–398 (2013).
2. M. M. Lee, J. Teuscher, T. Miyasaka, T. N. Murakami, H. J. Snaith, Efficient hybrid solar cells based on meso-superstructured organometal halide perovskites. *Science* **338**, 643–647 (2012).
3. A. Mei, X. Li, L. Liu, Z. Ku, T. Liu, Y. Rong, M. Xu, M. Hu, J. Chen, Y. Yang, M. Grätzel, H. Han, A hole-conductor–free, fully printable mesoscopic perovskite solar cell with high stability. *Science* **345**, 295–298 (2014).
4. H. Zhou, Q. Chen, G. Li, S. Luo, T.-b. Song, H.-S. Duan, Z. Hong, J. You, Y. Liu, Y. Yang, Interface engineering of highly efficient perovskite solar cells. *Science* **345**, 542–546 (2014).
5. W. S. Yang, J. H. Noh, N. J. Jeon, Y. C. Kim, S. Ryu, J. Seo, S. I. Seok, High-performance photovoltaic perovskite layers fabricated through intramolecular exchange. *Science* **348**, 1234–1237 (2015).
6. M. Saliba, S. Orlandi, T. Matsui, S. Aghazada, M. Cavazzini, J.-P. Correa-Baena, P. Gao, R. Scopelliti, E. Mosconi, K.-H. Dahmen, F. De Angelis, A. Abate, A. Hagfeldt, G. Pozzi, M. Graetzel, M. K. Nazeeruddin, A molecularly engineered hole-transporting material for efficient perovskite solar cells. *Nat. Energy* **1**, 15017 (2016).
7. G. Xing, N. Mathews, S. Sun, S. S. Lim, Y. M. Lam, M. Grätzel, S. Mhaisalkar, T. C. Sum, Long-range balanced electron- and hole-transport lengths in organic-inorganic $CH_3NH_3PbI_3$. *Science* **342**, 344–347 (2013).
8. T. M. Brenner, D. A. Egger, L. Kronik, G. Hodes, D. Cahen, Hybrid organic—inorganic perovskites: Low-cost semiconductors with intriguing charge-transport properties. *Nat. Rev. Mater.* **1**, 15007 (2016).
9. T. Etienne, E. Mosconi, F. De Angelis, Dynamical origin of the Rashba effect in organohalide lead perovskites: A key to suppressed carrier recombination in perovskite solar cells? *J. Phys. Chem. Lett.* **7**, 1638–1645 (2016).
10. O. Yaffe, Y. Guo, L. Z. Tan, D. A. Egger, T. Hull, C. C. Stoumpos, F. Zheng, T. F. Heinz, L. Kronik, M. G. Kanatzidis, J. S. Owen, A. M. Rappe, M. A. Pimenta, L. E. Brus, Local polar fluctuations in lead halide perovskite crystals. *Phys. Rev. Lett.* **118**, 136001 (2017).
11. C. Motta, F. El-Mellouhi, S. Kais, N. Tabet, F. Alharbi, S. Sanvito, Revealing the role of organic cations in hybrid halide perovskite $CH_3NH_3PbI_3$. *Nat. Commun.* **6**, 7026 (2015).
12. S. Liu, F. Zheng, N. Z. Koocher, H. Takenaka, F. Wang, A. M. Rappe, Ferroelectric domain wall induced band-gap reduction and charge separation in organometal halide perovskites. *J. Phys. Chem. Lett.* **6**, 693–699 (2015).
13. F. Zheng, L. Z. Tan, S. Liu, A. M. Rappe, Rashba spin–orbit coupling enhanced carrier lifetime in $CH_3NH_3PbI_3$. *Nano Lett.* **15**, 7794–7800 (2015).
14. M. Coll, A. Gomez, E. Mas-Marza, O. Almora, G. Garcia-Belmonte, M. Campoy-Quiles, J. Bisquert, Polarization switching and light-enhanced piezoelectricity in lead halide perovskites. *J. Phys. Chem. Lett.* **6**, 1408–1413 (2015).
15. J. M. Frost, K. T. Butler, F. Brivio, C. H. Hendon, M. van Schilfgaarde, A. Walsh, Atomistic origins of high-performance in hybrid halide perovskite solar cells. *Nano Lett.* **14**, 2584–2590 (2014).
16. X.-Y. Zhu, V. Podzorov, Charge carriers in hybrid organic–inorganic lead halide perovskites might be protected as large polarons. *J. Phys. Chem. Lett.* **6**, 4758–4761 (2015).
17. J. Ma, L.-W. Wang, Nanoscale charge localization induced by random orientations of organic molecules in hybrid perovskite $CH_3NH_3PbI_3$. *Nano Lett.* **15**, 248–253 (2015).
18. A. J. Neukirch, W. Nie, J.-C. Blancon, K. Appavoo, H. Tsai, M. Y. Sfeir, C. Katan, L. Pedesseau, J. Even, J. J. Crochet, G. Gupta, A. D. Mohite, S. Tretiak, Polaron stabilization by cooperative lattice distortion and cation rotations in hybrid perovskite materials. *Nano Lett.* **16**, 3809–3816 (2016).
19. W. Nie, J.-C. Blancon, A. J. Neukirch, K. Appavoo, H. Tsai, M. Chhowalla, M. A. Alam, M. Y. Sfeir, C. Katan, J. Even, S. Tretiak, J. J. Crochet, G. Gupta, A. D. Mohite, Light-activated photocurrent degradation and self-healing in perovskite solar cells. *Nat. Commun.* **7**, 11574 (2016).
20. N. Onoda-Yamamuro, T. Matsuo, H. Suga, Calorimetric and IR spectroscopic studies of phase transitions in methylammonium trihalogenoplumbates (II)†. *J. Phys. Chem. Solids* **51**, 1383–1395 (1990).
21. T. J. Jacobsson, L. J. Schwan, M. Ottosson, A. Hagfeldt, T. Edvinsson, Determination of thermal expansion coefficients and locating the temperature-induced phase transition in methylammonium lead perovskites using x-ray diffraction. *Inorg. Chem.* **54**, 10678–10685 (2015).
22. J. J. Choi, X. Yang, Z. M. Norman, S. J. L. Billinge, J. S. Owen, Structure of methylammonium lead iodide within mesoporous titanium dioxide: Active material in high-performance perovskite solar cells. *Nano Lett.* **14**, 127–133 (2014).
23. D. Li, G. Wang, H.-C. Cheng, C.-Y. Chen, H. Wu, Y. Liu, Y. Huang, X. Duan, Size-dependent phase transition in methylammonium lead iodide perovskite microplate crystals. *Nat. Commun.* **7**, 11330 (2016).
24. C. Xiao, C. Xiao, Z. Li, H. Guthrey, J. Moseley, Y. Yang, S. Wozny, H. Moutinho, B. To, J. J. Berry, B. Gorman, Y. Yan, K. Zhu, M. Al-Jassim, Mechanisms of electron-beam-induced

damage in perovskite thin films revealed by cathodoluminescence spectroscopy. *J. Phys. Chem. C* **119**, 26904–26911 (2015).
25. H. Yuan, E. Debroye, K. Janssen, H. Naiki, C. Steuwe, G. Lu, M. Moris, E. Orgiu, H. Uji-I, F. De Schryver, P. Samorì, J. Hofkens, M. Roeffaers, Degradation of methylammonium lead iodide perovskite structures through light and electron beam driven ion migration. *J. Phys. Chem. Lett.* **7**, 561–566 (2016).
26. A. M. A. Leguy, J. Moore Frost, A. P. McMahon, V. Garcia Sakai, W. Kockelmann, C. H. Law, X. Li, F. Foglia, A. Walsh, B. C. O'Regan, J. Nelson, J. T. Cabral, P. R. F. Barnes, The dynamics of methylammonium ions in hybrid organic-inorganic perovskite solar cells. *Nat. Commun.* **6**, 7124 (2015).
27. R. Srinivasan, V. A. Lobastov, C.-Y. Ruan, A. H. Zewail, Ultrafast electron diffraction (UED): A new development for the 4D determination of transient molecular structures. *Helv. Chim. Acta* **86**, 1763–1838 (2003).
28. R. P. Chatelain, V. R. Morrison, B. L. M. Klarenaar, B. J. Siwick, Coherent and incoherent electron-phonon coupling in graphite observed with radio-frequency compressed ultrafast electron diffraction. *Phys. Rev. Lett.* **113**, 235502 (2014).
29. V. R. Morrison, R. P. Chatelain, K. L. Tiwari, A. Hendaoui, A. Bruhács, M. Chaker, B. J. Siwick, A photoinduced metal-like phase of monoclinic VO_2 revealed by ultrafast electron diffraction. *Science* **346**, 445–448 (2014).
30. A. M. Lindenberg, J. Larsson, K. Sokolowski-Tinten, K. J. Gaffney, C. Blome, O. Synnergren, J. Sheppard, C. Caleman, A. G. Macphee, D. Weinstein, D. P. Lowney, T. K. Allison, T. Matthews, R. W. Falcone, A. L. Cavalieri, D. M. Fritz, S. H. Lee, P. H. Bucksbaum, D. A. Reis, J. Rudati, P. H. Fuoss, C. C. Kao, D. P. Siddons, R. Pahl, J. Als-Nielsen, S. Duesterer, R. Ischebeck, H. Schlarb, H. Schulte-Schrepping, T. Tschentscher, J. Schneider, D. von der Linde, O. Hignette, F. Sette, H. N. Chapman, R. W. Lee, T. N. Hansen, S. Techert, J. S. Wark, M. Bergh, G. Huldt, D. van der Spoel, N. Timneanu, J. Hajdu, R. A. Akre, E. Bong, P. Krejcik, J. Arthur, S. Brennan, K. Luening, J. B. Hastings, Atomic-scale visualization of inertial dynamics. *Science* **308**, 392–395 (2005).
31. E. M. Mannebach, R. Li, K.-A. Duerloo, C. Nyby, P. Zalden, T. Vecchione, F. Ernst, A. H. Reid, T. Chase, X. S. Shen, S. Weathersby, C. Hast, R. Hettel, R. Coffee, N. Hartmann, A. R. Fry, Y. Yu, L. Cao, T. F. Heinz, E. J. Reed, H. A. Dürr, X. Wang, A. M. Lindenberg, Dynamic structural response and deformations of monolayer MoS_2 visualized by femtosecond electron diffraction. *Nano Lett.* **15**, 6889–6895 (2015).
32. A. D. Wright, C. Verdi, R. L. Milot, G. E. Eperon, M. A. Pérez-Osorio, H. J. Snaith, F. Giustino, M. B. Johnston, L. M. Herz, Electron–phonon coupling in hybrid lead halide perovskites. *Nat. Commun.* **7**, 11755 (2016).
33. Y. Yang, D. P. Ostrowski, R. M. France, K. Zhu, J. van de Lagemaat, J. M. Luther, M. C. Beard, Observation of a hot-phonon bottleneck in lead-iodide perovskites. *Nat. Photonics* **10**, 53–59 (2015).
34. J. Feng, Mechanical properties of hybrid organic-inorganic $CH_3NH_3BX_3$ (B = Sn, Pb; X = Br, I) perovskites for solar cell absorbers. *APL Mater.* **2**, 81801 (2014).
35. T. M. Brenner, D. A. Egger, A. M. Rappe, L. Kronik, G. Hodes, D. Cahen, Are mobilities in hybrid organic-inorganic halide perovskites actually "high"? *J. Phys. Chem. Lett.* **6**, 4754–4757 (2015).
36. H. T. Yi, X. Wu, X. Zhu, V. Podzorov, Intrinsic charge transport across phase transitions in hybrid organo-inorganic perovskites. *Adv. Mater.* **28**, 6509–6514 (2016).
37. T. Chase, M. Trigo, A. H. Reid, R. Li, T. Vecchione, X. Shen, S. Weathersby, R. Coffee, N. Hartmann, D. A. Reis, X. J. Wang, H. A. Dürr, Ultrafast electron diffraction from non-equilibrium phonons in femtosecond laser heated Au films. *Appl. Phys. Lett.* **108**, 041909 (2016).
38. T. Baikie, Y. Fang, J. M. Kadro, M. Schreyer, F. Wei, S. G. Mhaisalkar, M. Graetzel, T. J. White, Synthesis and crystal chemistry of the hybrid perovskite $(CH_3NH_3)PbI_3$ for solid-state sensitised solar cell applications. *J. Mater. Chem. A* **1**, 5628–5641 (2013).
39. F. Brivio, J. M. Frost, J. M. Skelton, A. J. Jackson, O. J. Weber, M. T. Weller, A. R. Goñi, A. M. A. Leguy, P. R. F. Barnes, A. Walsh, Lattice dynamics and vibrational spectra of the orthorhombic, tetragonal, and cubic phases of methylammonium lead iodide. *Phys. Rev. B* **92**, 144308 (2015).
40. P. S. Whitfield, N. Herron, W. E. Guise, K. Page, Y. Q. Cheng, I. Milas, M. K. Crawford, Structures, phase transitions and tricritical behavior of the hybrid perovskite methyl ammonium lead iodide. *Sci. Rep.* **6**, 35685 (2016).
41. Y. Zhou, L. You, S. Wang, Z. Ku, H. Fan, D. Schmidt, A. Rusydi, L. Chang, L. Wang, P. Ren, L. Chen, G. Yuan, L. Chen, J. Wang, Giant photostriction in organic–inorganic lead halide perovskites. *Nat. Commun.* **7**, 11193 (2016).
42. D. A. Egger, L. Kronik, A. M. Rappe, Theory of hydrogen migration in organic-inorganic halide perovskites. *Angew. Chem. Int. Ed.* **54**, 12437–12441 (2015).
43. S. Liu, F. Zheng, I. Grinberg, A. M. Rappe, Photoferroelectric and photopiezoelectric properties of organometal halide perovskites. *J. Phys. Chem. Lett.* **7**, 1460–1465 (2016).
44. Y. Deng, Z. Xiao, J. Huang, Light-induced self-poling effect on organometal trihalide perovskite solar cells for increased device efficiency and stability. *Adv. Energy Mater.* **5**, 1500721 (2015).
45. C. Eames, J. M. Frost, P. R. F. Barnes, B. C. O'Regan, A. Walsh, M. S. Islam, Ionic transport in hybrid lead iodide perovskite solar cells. *Nat. Commun.* **6**, 7497 (2015).
46. D. W. deQuilettes, W. Zhang, V. M. Burlakov, D. J. Graham, T. Leijtens, A. Osherov, V. Bulović, H. J. Snaith, D. S. Ginger, S. D. Stranks, Photo-induced halide redistribution in organic–inorganic perovskite films. *Nat. Commun.* **7**, 11683 (2016).
47. E. J. Juarez-Perez, R. S. Sanchez, L. Badia, G. Garcia-Belmonte, Y. S. Kang, I. Mora-Sero, J. Bisquert, Photoinduced giant dielectric constant in lead halide perovskite solar cells. *J. Phys. Chem. Lett.* **5**, 2390–2394 (2014).
48. S. P. Weathersby, G. Brown, M. Centurion, T. F. Chase, R. Coffee, J. Corbett, J. P. Eichner, J. C. Frisch, A. R. Fry, M. Gühr, N. Hartmann, C. Hast, R. Hettel, R. K. Jobe, E. N. Jongewaard, J. R. Lewandowski, R. K. Li, A. M. Lindenberg, I. Makasyuk, J. E. May, D. McCormick, M. N. Nguyen, A. H. Reid, X. Shen, K. Sokolowski-Tinten, T. Vecchione, S. L. Vetter, J. Wu, J. Yang, H. A. Dürr, X. J. Wang, Mega-electron-volt ultrafast electron diffraction at SLAC National Accelerator Laboratory. *Rev. Sci. Instrum.* **86**, 73702 (2015).
49. S. Plimpton, Fast parallel algorithms for short-range molecular dynamics. *J. Comput. Phys.* **117**, 1–19 (1995).
50. A. Mattoni, A. Filippetti, M. I. Saba, P. Delugas, Methylammonium rotational dynamics in lead halide perovskite by classical molecular dynamics: The role of temperature. *J. Phys. Chem. C* **119**, 17421–17428 (2015).
51. C. C. Stoumpos, C. D. Malliakas, M. G. Kanatzidis, Semiconducting tin and lead iodide perovskites with organic cations: Phase transitions, high mobilities, and near-infrared photoluminescent properties. *Inorg. Chem.* **52**, 9019–9038 (2013).
52. J. Yin, D. Cortecchia, A. Krishna, S. Chen, N. Mathews, A. C. Grimsdale, C. Soci, Interfacial charge transfer anisotropy in polycrystalline lead iodide perovskite films. *J. Phys. Chem. Lett.* **6**, 1396–1402 (2015).
53. L.-M. Peng, Electron scattering factors of ions and their parameterization. *Acta Crystallogr.* **54**, 481–485 (1998).
54. L.-M. Peng, G. Ren, S. L. Dudarev, M. J. Whelan, Robust parameterization of elastic and absorptive electron atomic scattering factors. *Acta Cryst.* **52**, 257–276 (1996).
55. B. J. Siwick, J. R. Dwyer, R. E. Jordan, R. J. D. Miller, An atomic-level view of melting using femtosecond electron diffraction. *Science* **302**, 1382–1385 (2003).
56. M. I. Saidaminov, A. L. Abdelhady, B. Murali, E. Alarousu, V. M. Burlakov, W. Peng, I. Dursun, L. Wang, Y. He, G. Maculan, A. Goriely, T. Wu, O. F. Mohammed, O. M. Bakr, High-quality bulk hybrid perovskite single crystals within minutes by inverse temperature crystallization. *Nat. Commun.* **6**, 7586 (2015).

Acknowledgments

Funding: This work was supported by the Department of Energy, Basic Energy Sciences, Materials Sciences and Engineering Division. The UED source was supported in part by the DOE BES Scientific User Facilities Division and the SLAC UED/UEM program development fund. X.Z. acknowledges the US Department of Energy, Office of Science - Basic Energy Sciences, Grant ER46980 for supporting the growth of the hybrid perovskite samples used in this study. L.Z.T. and A.M.R. acknowledge support from the Office of Naval Research under grant number N00014-17-1-2574. D.A.E. and L.K. were supported by the Austrian Science Fund (FWF): J3608–N20 and by a research grant from Dana and Yossie Hollander, in the framework of the WIS Sustainability and Energy Research Initiative. T.H. acknowledges support from the Precourt Institute for Energy. H.I.K. thanks the Alfred P. Sloan Foundation for support. M.D.S. is supported by an NSF Graduate Research Fellowship (DGE-114747). Part of this work was performed at the Stanford Nano Shared Facilities (SNSF), supported by the NSF under award ECCS-1542152. **Author contributions:** X. Wu, X.S., T.H., R.L., R.C., I.M., Q.Z., A.F., J.S.R., X. Wang, and A.M.L. carried out the UED experiment. X. Wu, K.M., M.T.T., M.D.S., B.G., H.I.K., and X.Z. led the sample growth, x-ray, and optical characterization experiments. L.Z.T., D.A.E., L.K., S.L., and A.M.R. carried out the theory and simulations. X. Wu and A.M.L. performed the data analysis and wrote the manuscript with input from all authors. **Competing interests:** The authors declare that they have no competing interests. **Data and materials availability:** All data needed to evaluate the conclusions in the paper are present in the paper and/or the Supplementary Materials. Additional data related to this paper may be requested from the authors. Correspondence and requests for materials should be addressed to A.M.L. at aaronl@stanford.edu.

Submitted 28 September 2016
Accepted 22 June 2017
Published 26 July 2017
10.1126/sciadv.1602388

Citation: X. Wu, L. Z. Tan, X. Shen, T. Hu, K. Miyata, M. T. Trinh, R. Li, R. Coffee, S. Liu, D. A. Egger, I. Makasyuk, Q. Zheng, A. Fry, J. S. Robinson, M. D. Smith, B. Guzelturk, H. I. Karunadasa, X. Wang, X. Zhu, L. Kronik, A. M. Rappe, A. M. Lindenberg, Light-induced picosecond rotational disordering of the inorganic sublattice in hybrid perovskites. *Sci. Adv.* **3**, e1602388 (2017).